



# Annealed PCz/MnO<sub>2</sub> nanocomposite for the methodical separation of photoinduced electron–hole pairs for escalated photocatalytic activity

Mubarak Ali Muhamath Basha<sup>1</sup> · John Williams David Nagarajan<sup>1</sup>

Received: 30 July 2021 / Accepted: 6 October 2021 / Published online: 4 November 2021  
© The Polymer Society, Taipei 2021

## Abstract

Polycarbazole (PCz) and polycarbazole (PCz)/manganese dioxide (MnO<sub>2</sub>) nanocomposite (PCM) were prepared by facile in-situ polymerization route. Variations in optical properties, crystal phase, morphology and surface area were observed which offers promising strategies for using annealed PCM for photocatalytic applications. The band gap energy is measured from the cyclic voltametry (CV) (PCz = 0.95 eV; MnO<sub>2</sub> = 0.9 eV). The XRD study shows that the β-MnO<sub>2</sub> incorporated in PCM is transformed into α and γ-MnO<sub>2</sub> due to the effect of annealing. The surface area of annealed PCM (33.8 m<sup>2</sup>/g) is 7.04 times higher than unannealed materials (4.8 m<sup>2</sup>g<sup>-1</sup>). The annealed PCM manifested uniform spherical morphology and exhibited excellent degradation efficiency towards RB dye under UV (96.2%) and natural sunlight (97.9%). Similarly, MG dye achieved the degradation efficiency of 97.4% and 98.3% under UV and natural sunlight. Furthermore, the radical trapping experiment evidenced that the superoxide (\*O<sub>2</sub><sup>-</sup>) and hydroxyl radicals (\*OH) played a dominating role in the photo degradation of RB and MG dyes. The present study imparts new enlightenment for the fabrication of reliable, inexpensive and exceptionally efficient photo catalyst for the elimination of hazardous textile dyes from the industrial waste water.

**Keywords** MnO<sub>2</sub> · Photo catalyst · Nanocomposite · Degradation · Rose Bengal · Malachite green

## Introduction

Recently, the water pollution has turned into a very critical issue because it inhibits the sustainable growth continuously due to the population explosion and rapid industrialization [1, 2]. Contaminated water contains toxic organic compounds which have major impact on human health and the environment which are carcinogenic and teratogenic [3]. Rose bengal (RB) is one of the important textile dye with a molecular formula of C<sub>20</sub>H<sub>2</sub>Cl<sub>4</sub>Na<sub>2</sub>O<sub>5</sub>. It is highly toxic and affects the corneal epithelium of the eyes, causes redness, inflammation and itching [4, 5]. In addition, malachite green (MG) is also an essential textile dye with the molecular formula of C<sub>23</sub>H<sub>25</sub>N<sub>2</sub>Cl, water soluble and known as basic green4 or Victorian greenB. It is extensively used in the dye industry and causes cancer and gene damage [6].

In recent years, photo catalysis as an inexpensive and eco-friendly technique has gained significant interest for the degradation of toxic pollutants discharged from the industries [7, 8]. The key emphasis in this technique is the selection of appropriate photo catalyst which responds to light irradiation because when the photocatalyst is irradiated with light it produces electron–hole (e<sup>-</sup>/h<sup>+</sup>) pairs for the degradation of toxic pollutants into H<sub>2</sub>O, CO<sub>2</sub> and other small molecules without the loss of the photocatalyst [9–12].

Recently the conjugated microporous polymers (crystalline porous organic material) were emerged as potential material for dye removal. They possess high surface area and thermal stability [13, 14]. Among them the polycarbazole based photo catalysts has been identified as an ideal candidate for the degradation of various dyes due to its unique properties. The PCz act as photosensitizer and inhibits the recombination of electron hole pairs. Furthermore, the delocalized π-conjugated system in PCz is beneficial to accelerate charge separation which improves the separation efficiency of light induced electron–hole pairs for enhanced photocatalytic activity. In addition, it possesses semiconducting behavior due to its conjugated structure. Thus, the

✉ Mubarak Ali Muhamath Basha  
mubarakscience@gmail.com

<sup>1</sup> Department of Chemistry, Chikkaiah Naicker College, Erode-638004, Tamil Nadu, India

combination of metal oxide and PCz matrix is expected to enable the separation of light induced electron–hole pairs. Besides, it is notable that the polycarbazole when combined with metaloxides are more advantageous for the photocatalytic applications. In addition to these, various polycarbazole based nanocomposites such as polycarbazole incorporated  $\text{TiO}_2$  nanocomposite [15], polycarbazole (PCz)/cuprous oxide ( $\text{Cu}_2\text{O}$ ) nanocube composite [16] and polycarbazole (PCz)/graphitic carbon nitride ( $\text{g-C}_3\text{N}_4$ ) [17] nanocomposites were reported as an effective photocatalyst for the degradation of various organic dyes under various light sources.

Among the various metal oxides, the  $\text{MnO}_2$  is extensively used for its excellent qualities such as cheap, nontoxic, resistance to acids, etc. Furthermore, it has the potential to eliminate the toxic pollutants present in the waste water. To date, various  $\text{MnO}_2$  incorporated photo catalyst such as PANI/ $\text{MnO}_2$  nanocomposite [18], PEDOT/ $\text{MnO}_2$  nanocomposite [19], bismuth oxyiodide ( $\text{BiOI}$ )/Manganese dioxide ( $\text{MnO}_2$ ) composite [20] and  $\text{Fe}_3\text{O}_4/\text{MnO}_2/\text{Mn}_3\text{O}_4$  [21] composite were considered as a potential materials for addressing the environmental issues.

Furthermore, the physical properties of the polymer nanocomposites can be improved by heat treatment which in turn enhances the photo catalytic activity [22, 23]. It is noteworthy that the p-n heterojunction photo catalyst will enable the separation of light induced electron–hole pair for the enhanced photo catalytic performance. Herein,  $\text{MnO}_2$  (n) is dispersed into polycarbazole (p) matrix for the construction of p-n heterojunction to improve the degradation of dyes.

The aim of the current investigation is to fabricate PCz and PCz/ $\text{MnO}_2$  nanocomposite by facile chemical route. The systematic study on the impact of annealing on the material properties as well as photo catalytic activity was studied. The PCz as a coating material over  $\text{MnO}_2$  was characterized by various state of the art techniques. The functional groups of PCM were determined by using fourier transform infrared (FTIR) technique. The field emission scanning electron microscope (FE-SEM) and high resolution transmission electron microscope (HRTEM) techniques were used to examine the morphology. The elements present in the material were identified by energy dispersive x-ray (EDX) spectrometer. The optical property was inspected by employing ultra violet diffuse reflectance spectroscopy (UV-DRS). The average crystallite size, crystal structure and crystallinity were analysed by x-ray diffraction (XRD) analysis. The physical properties of PCM were studied by burnauer-emmett-teller (BET) analysis. Thermal studies were scrutinized by thermo gravimetric-differential thermal analysis (TG–DTA). The photo catalytic performance of PCM was analyzed by degrading the RB and MG dyes under UV and direct sunlight illumination. Furthermore, recycling test, scavenging test and textile effluent sample analysis were investigated. The extent of mineralization and degradation

of the organic dyes were examined by employing chemical oxygen demand (COD) and total organic carbon (TOC) analysis.

## Experimental section

### Materials

Manganese dioxide ( $\text{MnO}_2$ ), carbazole, methanol, acetone and ammonium peroxydisulfate (APS) were of analytical grade and acquired from Merck. EDTA, p-benzoquinone, isopropyl alcohol, RB and MG dyes from S D Fine-Chem. Deionized water was utilized for synthesis and photo catalytic experiments.

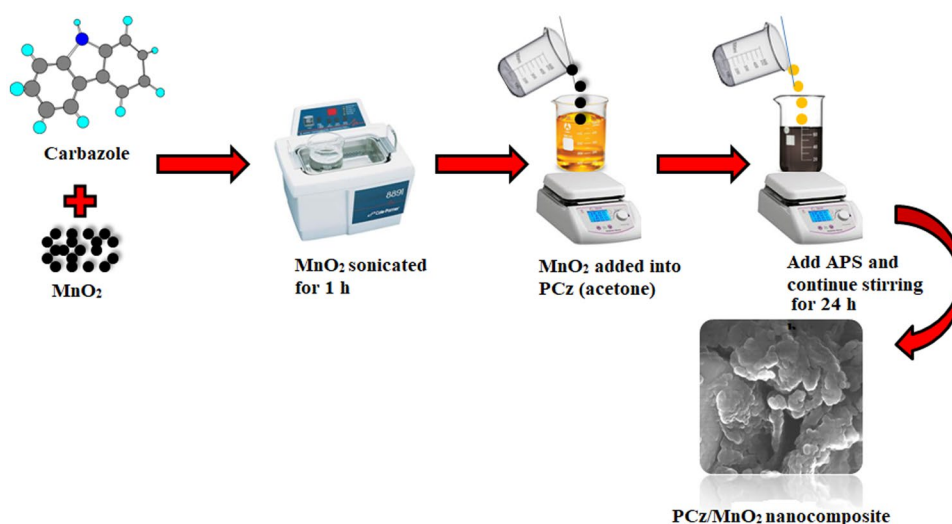
### Synthesis of polycarbazole and polycarbazole- $\text{MnO}_2$ nanocomposite

The PCz/ $\text{MnO}_2$  nanocomposite was fabricated by facile in situ chemical oxidative polymerization route. The 1 g of  $\text{MnO}_2$  is added to a beaker containing 100 ml acetone and ultrasonicated for 1 h. The sonicated solution is added drop wise into the carbazole solutions, agitated vigorously for 4 h in order to adsorb the  $\text{MnO}_2$  nanoparticles into carbazole monomer. Further the oxidant ammonium per sulphate (APS) is added drop wise with continuous stirring for 24 h at room temperature ( $25 \pm 5^\circ\text{C}$ ). These results in the polymerization of carbazole and the  $\text{MnO}_2$  nanoparticles are adsorbed which is identified by brown colour. The precipitate thus formed is filtered, washed several times with methanol to get rid of the impurities (unreacted APS), dried up at  $60^\circ\text{C}$  for 2 h in oven and milled into fine powder. The polycarbazole (PCz) was fabricated in the aforementioned procedure without adding  $\text{MnO}_2$ . The synthesis strategy of PCz/ $\text{MnO}_2$  nanocomposite is graphically illustrated in Scheme 1. The PCM is annealed at various time intervals and temperatures such as  $300^\circ\text{C}$  for 5 h (PCM1),  $300^\circ\text{C}$  for 10 h (PCM2),  $600^\circ\text{C}$  for 5 h (PCM3) and  $600^\circ\text{C}$  for 10 h (PCM4).

### Characterization of polycarbazole- $\text{MnO}_2$ nanocomposite

The structure, elemental composition and morphology of the synthesized material were identified by the following analytical techniques. The fourier transform infrared spectrometer (Perkin Elmer, USA) is used to identify the functional groups. The optical studies were carried out by using UV-DRS spectrophotometer (varian, Cary 5000) and the band gap was calculated by applying Kubelka–Munk equation.

**Scheme 1** Graphical illustration of the synthesis of PCz/MnO<sub>2</sub> nanocomposite



$$F(R) = \frac{1 - R^2}{2R} = \frac{\alpha}{s} \quad (1)$$

$F(R)$  = Kubelka–Munk function,  $R$  is reflectance,  $\alpha$  is absorption coefficient and  $s$  is scattering coefficient. The band gap of semiconductors was calculated by employing absorption coefficient equation.

$$(h\nu\alpha)^{1/n} = A(h\nu - E_g) \quad (2)$$

In this equation,  $\alpha$  is adsorption coefficient,  $h$  is plank's constant,  $\nu$  is vibrational frequency and  $E_g$  is band gap. In case of indirect band semiconductor the value of  $n$  is 2. The average crystallite size, crystal structure and crystallinity were studied by employing powder x-ray diffraction (PXRD) on Bruker AXS D8 Advance X-ray diffractometer with Cu-K $\alpha$  radiation ( $\lambda = 1.5406 \text{ \AA}$ ). The morphological characteristics of the material were examined by field emission scanning electron microscope (Sigma with Gemini column) and possess high resolution of 1.5 nm. The elements present in the material and the color mapping was analysed by energy dispersive X-ray spectrometer (Nano Xflash detector, bruker). The morphology is further examined by high resolution transmission electron microscope (HR-TEM, JEOL 2100) operated at 300 kV. The TGA/DTA was performed by using Perkin Elmer STA 6000, Diamond TG/DTA. The surface area, mean pore diameter and pore volume were measured by using Belsorp mini 2 (adsorption temperature is 77 K at saturated vapour pressure of 97.708 kPa). HOMO–LUMO energy level of PCz and MnO<sub>2</sub> was measured by cyclic voltammetry (Auto lab) using platinum (Pt) electrodes at a sweep rate of 20mVs<sup>-1</sup>.

### Analysis of photo catalytic performance

The photo degradation performance of RB and MG dyes over the as-synthesized material was evaluated under UV light (30 W, length 60 cm) and natural sunlight (10:30 am to 3:00 pm). The Lutron UV light meter (UV-340A) was used to calculate the mean UV light and solar intensity throughout the photo catalytic experiment (2290 uW/cm<sup>2</sup>: sunlight; 850 uW/cm<sup>2</sup>: UV light). Prior to illumination, the dye solution is stirred under dark medium at 25 °C for 30 min to reach the adsorption–desorption equilibrium. The PCM (100 mg) was dissipated in 100 ml of aqueous dye suspension (RB: 10 mg L<sup>-1</sup> and MG: 10 mg L<sup>-1</sup>) with constant stirring. The aliquot of the degraded dye suspension is withdrawn at regular interval of time, centrifuged at 400 rpm and monitored by UV–vis spectrum. The degradation percentage was measured by applying the equation given below,

$$\text{Degradation percentage (\%)} = \frac{(C_o - C)}{C_o} \times 100 \quad (3)$$

where,  $C_o$  is the initial dye concentration of the dye before irradiation, and  $C$  is the concentration of dye after time  $t$ . The above equation is used to calculate the efficiency of the degraded dye. The kinetic study of the photo degraded dyes is carried out at various time intervals by Langmuir–Hinshelwood (L–H) model; the apparent rate constant is calculated by employing the equation provided below.

$$K_{app} = \ln \frac{C_o}{C_t} \quad (4)$$

Herein, the  $k_{app}$  is the rate constant of pseudo first order and  $t$  is the time interval. The  $k_{app}$  is determined from the slope by plotting the graph between  $\ln(C_0/C_t)$  and  $t$ .  $C_0$  is the initial dye concentrations after adsorption under dark (30 min) and  $C_t$  is the concentration of dyes at various time intervals. Furthermore, the mineralization of the organic pollutants into intermediate products which are finally mineralized into  $CO_2$  and  $H_2O$  by the hydroxyl radical or the photo generated hole cannot be evaluated by the spectroscopic techniques. Therefore, the TOC analysis is carried out and its mineralization efficiency was studied by using the equation given below.

$$\text{Mineralization efficiency (\%)} = \frac{(TOC_o - TOC_t)}{TOC_o} \times 100 \quad (5)$$

Herein, the  $TOC_o$  and  $TOC_t$  corresponds to TOC concentrations before and after the reaction. The photo stability study was investigated by using the material from the degraded dye. It was filtered off after each cycle washed with methanol, deionized water, dried and used for the next cycle. Furthermore, to understand the key radicals involved in photo degradation, radical-trapping experiments was performed. Isopropyl alcohol (IPA), Ethylenediaminetetraacetic acid disodium salt (EDTA-2Na) and p-benzoquinone (BQ) were functioned as scavengers of hydroxyl ( $\cdot OH$ ), holes ( $h^+$ ) and superoxide ( $\cdot O_2^-$ ) species.

The textile effluent sample analysis was performed by using the reactive black dye. The dye effluent is fetched from the textile industry located in Erode (Tamilnadu, India). The photo catalytic activity of textile effluent sample is evaluated under direct sunlight. The as prepared material (100 mg) was dissipated in 100 ml of dye suspension (Textile effluent sample:  $10 \text{ ml L}^{-1}$ ) with constant stirring. The aliquot of the degraded dye solution is withdrawn at regular interval and monitored by UV technique. Furthermore the chemical oxygen demand (COD) technique is used to evaluate the quality of the degraded sample by employing dichromate reflux method.

## Results & discussions

### Fourier transform infrared (FTIR) analysis

The FTIR spectrum of PCz,  $\beta$ -MnO<sub>2</sub> and PCM is displayed in Fig. 1. The N–H and O–H stretching vibration peaks for PCz is appeared at 3420.2 and 3048.9  $\text{cm}^{-1}$  [24]. The bands observed at 1593.8 and 1443.3  $\text{cm}^{-1}$  were ascribed to the benzenoid and quinonoid units. The peaks formed at 921.5, 851.2 and 718.8  $\text{cm}^{-1}$  were attributed to the emergence of

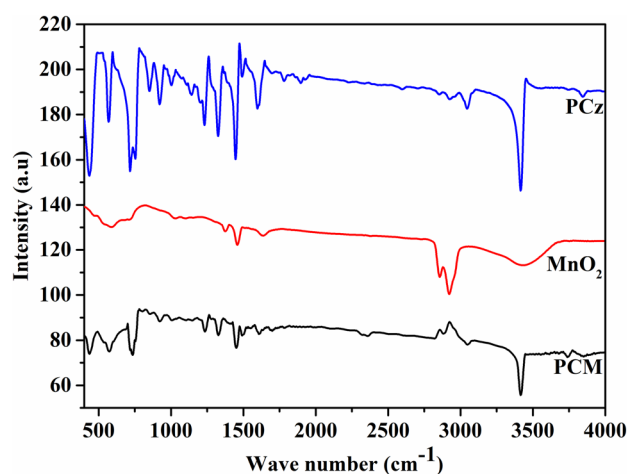


Fig. 1 FTIR spectrum of PCz,  $\beta$ -MnO<sub>2</sub> and PCM

unsubstituted carbazole, implying that the polymerization taken from 3 to 6<sup>th</sup> position. The results agreed well with the reported literature [25].

On the other hand, the FTIR spectrum of PCM is significantly changed after the decoration of MnO<sub>2</sub> into PCz matrix. The O–H and N–H stretching vibration is appeared at 3044.3 and 3418.7  $\text{cm}^{-1}$ . The peaks formed at 924.7 and 847.8  $\text{cm}^{-1}$  were corroborated to the emergence of unsubstituted carbazole. The band formed at 1593 and 1489.6  $\text{cm}^{-1}$  were related to the quinonoid and benzenoid units. The results obtained were in good consistent with the earlier studies [26–29]. A broad peak at 584.1  $\text{cm}^{-1}$  is observed for pure  $\beta$  MnO<sub>2</sub>. In addition, the peaks observed between 2800–2900  $\text{cm}^{-1}$  was shifted to the lower wave numbers and the percentage transmittance is decreased which is due to the loading of PCz [15]. But in the case of PCM, it is shifted to 572  $\text{cm}^{-1}$ . The broad peak appeared for MnO<sub>2</sub> is due to the interaction between the oxygen molecules of MnO<sub>2</sub> and N–H bonds of PCz. The shifting of the peaks to lower and higher wave number is due to the synergistic effect between the PCz and MnO<sub>2</sub> which is more advantageous for the transport of charge carriers for enhanced photo catalytic activity.

### Optical studies

The optical properties of PCz and PCM were studied by UV-DRS technique and illustrated in Fig. 2a. The absorption position of pure PCz is observed at 326.3 nm. Whereas, the PCM shows the peak at 375.7 nm which is distinctly red shift. The apparent band gaps were estimated by using Kubelka–Munk method as illustrated in Fig. 2b. The band gap of pure PCz is 3.8 eV, whereas for PCM it is calculated as 3.54 eV which is decreased after the introduction of

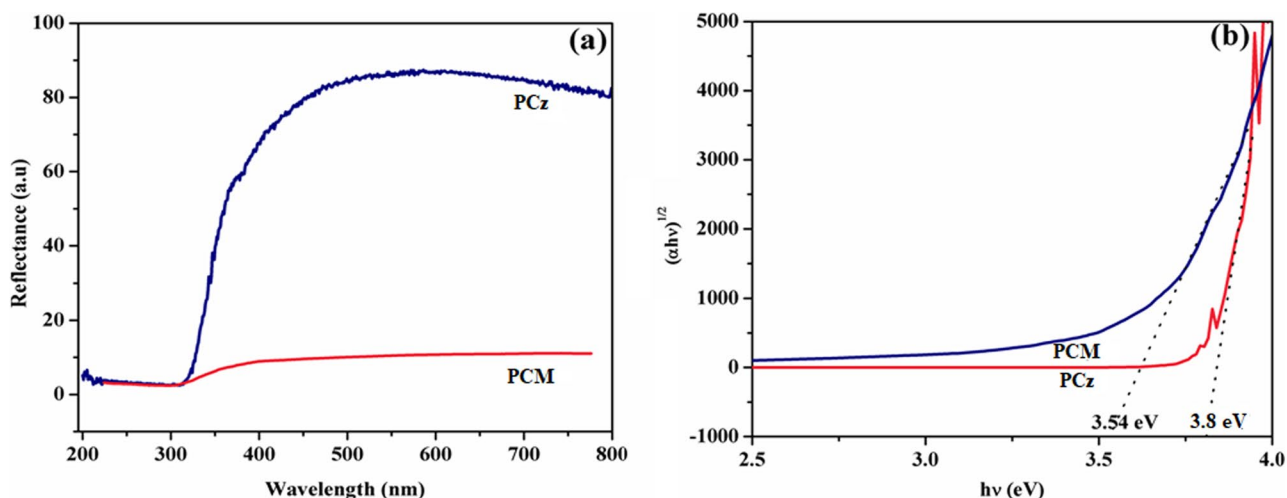


**Fig. 2** UV-DRS spectrum of (a) PCz (b) PCM and Kubelka–Munk plot (inset) of PCz and PCM

MnO<sub>2</sub> in the nanocomposite matrix. The decrease in the band gap of PCM is owing to the emergence of sub-band level connecting the conduction and valence band due to the incorporation of MnO<sub>2</sub> into PCz matrix [30]. The Fig. S1 (Supplementary files) shows the UV absorption spectrum of the annealed samples. It is observed that the annealed samples show low absorption peaks in the near UV spectral region between 300 to 400 nm and exhibited red shift due to the increase in the temperature. The band gap ( $E_g$ ) of the annealed material exhibited increase in the band gap from 3.54 (PCM) to 3.79 eV (PCM1). The increase in the  $E_g$  values is due to the following facts. The first one is the crystallinity is increased on account of annealing at higher temperatures (300 °C and 600 °C). In addition, the grain boundaries started to decrease which led to the fast reduction of defect states which results in the increased  $E_g$  values. On the other hand, further increase in the annealing temperature decreases the band gap from 3.79 (PCM1) to 3.67 eV (PCM2) and 3.65 eV (PCM3 and PCM4). The annealed PCM exhibited red shift towards longer wavelength due to the crystalline nature of the material which decreased the band gap value [31].

## X-ray diffraction

The pXRD pattern of PCz, MnO<sub>2</sub>, PCM, PCM1, PCM2, PCM3 and PCM4 were depicted in Fig. 3(a–g). The pure PCz (Fig. 3a) shows five prominent peaks appeared at 18.5°, 19.2°, 19.8°, 23.3° and 28°. The pronounced peak appeared at 18.527° is assigned to the PCz backbone. The MnO<sub>2</sub> (Fig. 3b) exhibited three distinct characteristic peaks at (2 $\theta$ ) 28.6°, 37.3° and 56.6° which corresponds to (110), (101) and (211) crystal planes. The planes indicate the face

centered cubic (FCC) crystal lattice and the peaks obtained are indexed to the pure phase of pyrolusite-MnO<sub>2</sub> (JCPDS NO: 24–0735). The sharp diffraction peaks observed for PCM (Fig. 3c), PCM1 (Fig. 3d) and PCM2 (Fig. 3e) are very close to  $\beta$ -MnO<sub>2</sub> and low intense peaks are obtained for PCz due to its amorphous nature. Furthermore, there is no evidence of impurity phases (such as  $\alpha$ ,  $\delta$ -MnO<sub>2</sub>) was detected.

On the other hand, the PCM3 (Fig. 3f) shows peaks at 28.7° (310), 32.7° (101), 36.5° (400) and 38.8° (330) which is indexed to  $\alpha$ -MnO<sub>2</sub> (JCPDS card No: 72–1982). The result suggests that the  $\alpha$ -MnO<sub>2</sub> phase was developed and dominated over  $\beta$ -MnO<sub>2</sub> in the PCM3 during annealing at high temperatures. In addition, the diffraction peaks for PCM4 (Fig. 3g) were presented at 26.6° (201), 36.5° (210), 38.2° (002) and 49.7° (410) which corresponds to  $\gamma$ -MnO<sub>2</sub> (JCPDS

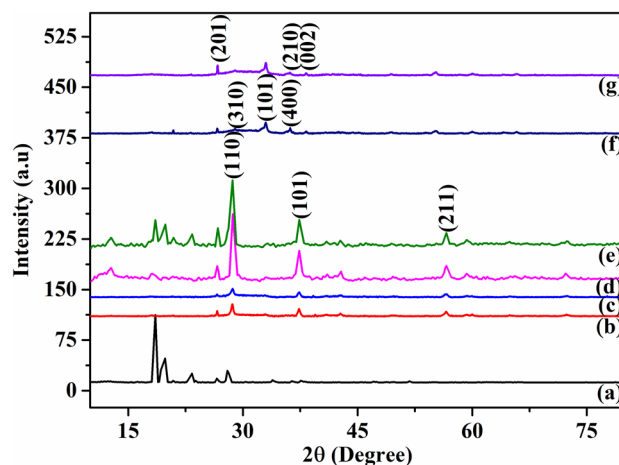


**Fig. 3** pXRD pattern of (a) PCz, (b) MnO<sub>2</sub>, (c) PCM, (d) PCM1, (e) PCM2, (f) PCM3 and (g) PCM4

card no: 42–1316). It is observed that the annealing of the material at higher temperatures results in the polymorphs of  $\text{MnO}_2$ . Furthermore, the PCM1, PCM2, PCM3 and PCM4 shows high crystallinity which is attributed to the fact that the intensity of the XRD crystalline peaks increases with the increase in the temperature from 300 °C to 600 °C suggesting the improvement in the crystallinity of the samples. When the temperature is increased the diffraction peaks are more distinct and the FWHM values narrows which indicates that the increase of crystallinity and the mean grain size [32]. The crystallite size of PCz, PCM, PCM1, PCM2, PCM3 and PCM4 were 62.44, 26.12, 24.30, 28.67, 26.64 and 28.82 nm respectively.

### Morphology and micro structural analysis

The morphology of the material plays a crucial role in governing the photo catalytic activity. Therefore the morphology of the as synthesized and annealed material is studied by SEM analysis and depicted in Fig. 4. The SEM image of PCz (Fig. 4a) shows irregular particles with agglomeration owing to the large surface area of the particles. On the other hand, the SEM images of

PCM (Fig. 4b) exhibits uniform globular like structure due to the surface modifications by incorporating  $\text{MnO}_2$  nanoparticles into the PCz matrix. The images revealed the high degree of structural uniformity and the agglomeration were reduced significantly which is expected to increase the surface area thereby enhances the photo degradation. These results are consistent with the previous studies [33]. The morphology of the material is improved after annealing which can be clearly seen from the FESEM analysis. The PCM1 (Fig. 4c) shows nano flakes like morphology, PCM2 (Fig. 4d) exhibited uniform spherical morphology, PCM3 (Fig. 4e) shows uniform globular like morphology and PCM4 (Fig. 4f) shows uniform globular particles with aggregation. The particles of PCM3 (128 nm) and PCM4 (176 nm) is started to agglomerate and becomes larger than PCM1 (78 nm) and PCM2 (89 nm). When the annealing temperature increased from 300 °C to 600 °C the small molecules acquires more kinetic energy and resulted in high molecular motion which in turn increases the grain size (clusters). In addition, the increasing of annealing time from 5 to 10 h resulted in randomly oriented aggregated particles due to the generation of excess kinetic energy to the particles at very high temperature. The result obtained agreed well with the previous reported literature [34].

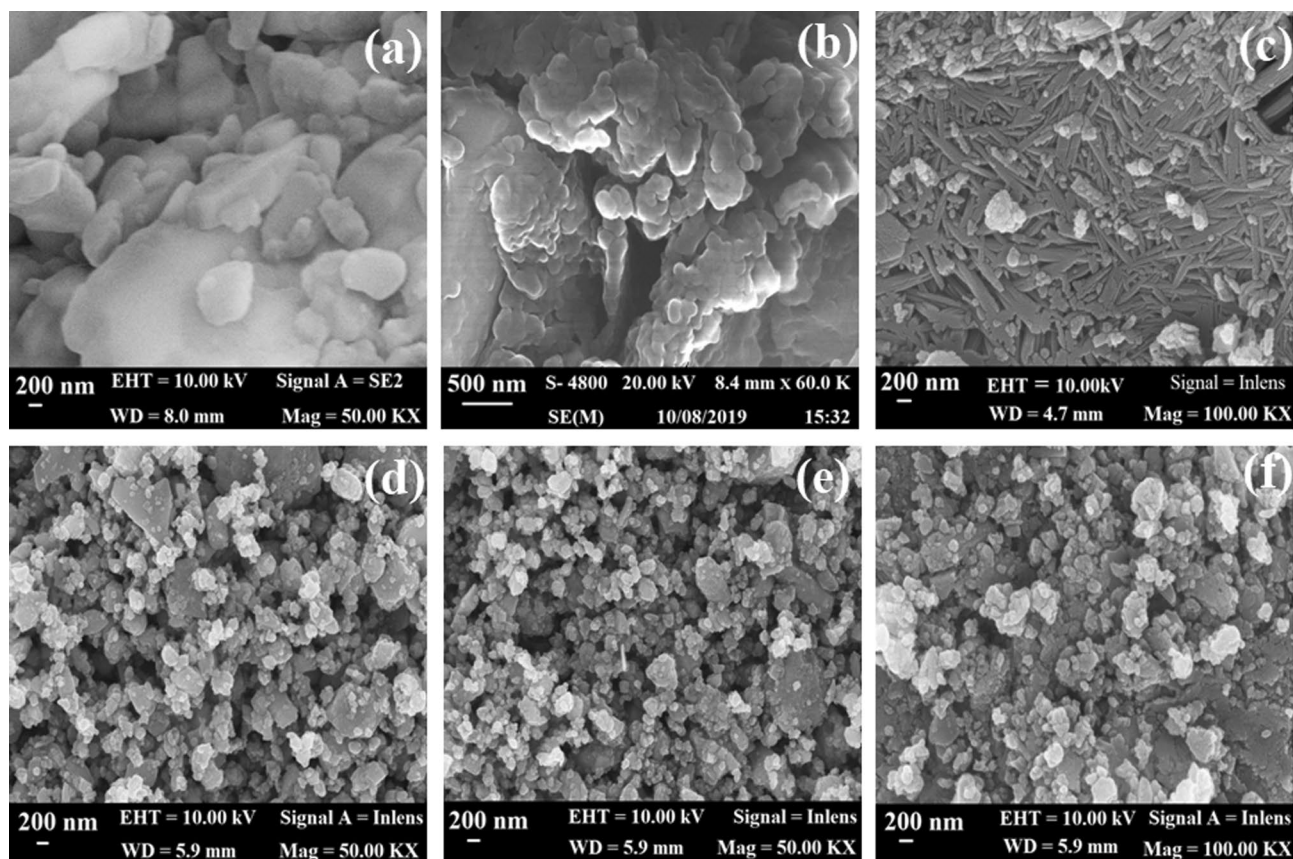


**Fig. 4** FESEM images of (a) PCz (b) PCM (c) PCM1 (d) PCM2 (e) PCM3 and (f) PCM4

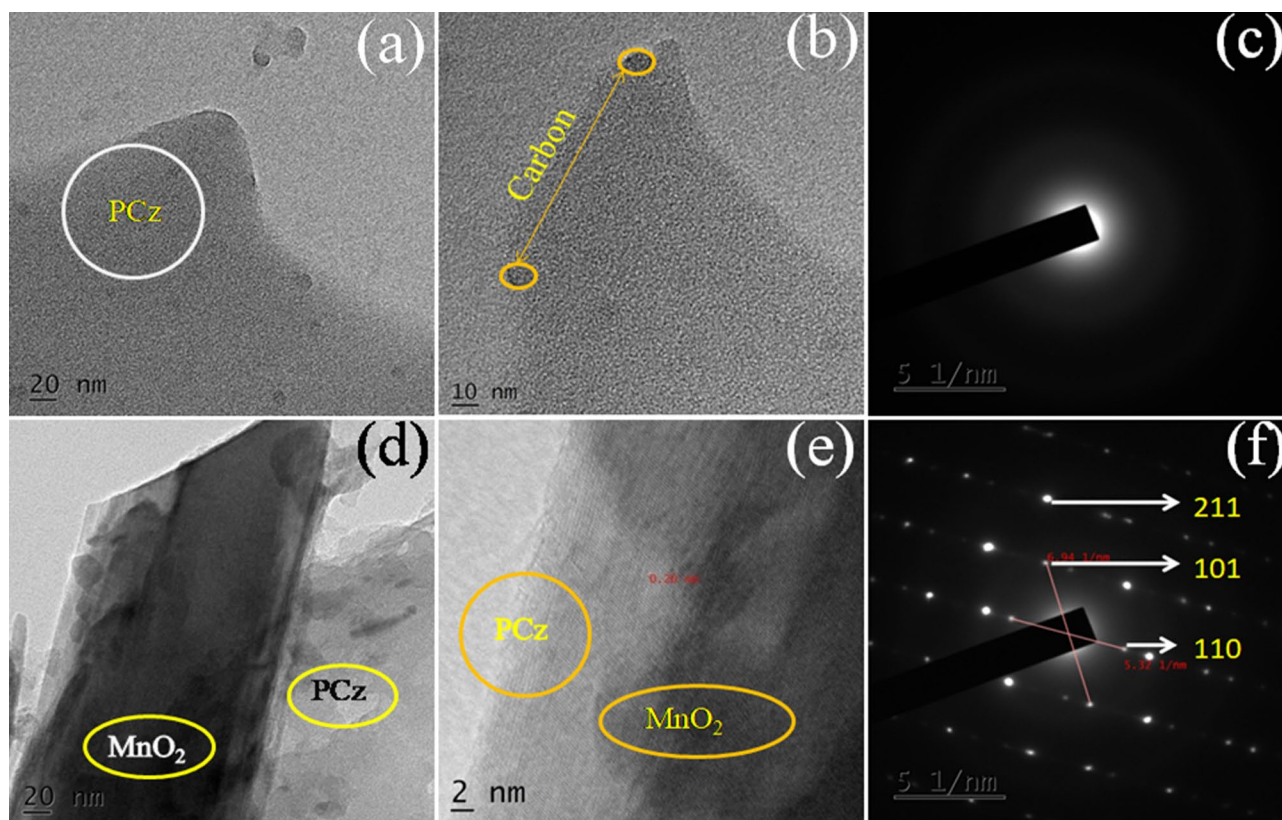


**Fig. 5** HRTEM image of (a–b) PCz and (d–e) PCM. SAED pattern of (c) PCz and (f) PCM

The HRTEM image of PCz (Fig. 5a) exhibited light phase mainly composed of carbon which is evidenced by FTIR, XRD and SEM-EDAX analysis. The lattice fringe of PCz (Fig. 5b) is not clear due to the amorphous nature. The SAED pattern of the PCz is shown in Fig. 5c. On the other hand, the PCM clearly displayed the interface between the PCz and MnO<sub>2</sub> with two distinct contrast phases. The dark region evidenced the presence of MnO<sub>2</sub> nanoparticles which is encapsulated by the light colored region corresponds to the polycarbazole backbone. As shown in Fig. 5d, the HRTEM images revealed the microscopic contact between the PCz and MnO<sub>2</sub> which results in the formation of PCz/MnO<sub>2</sub> nanocomposite. The Fig. 5e shows the well determined lattice space indexed to the face centered cubic (FCC). The interplanar spacing between the two adjacent lattice planes is 0.28 and 0.37 nm which is assigned to the 101 and 110 planes of  $\beta$ -MnO<sub>2</sub>. The results observed were consistent with the d spacing values of the XRD pattern of  $\beta$ -MnO<sub>2</sub> (JCPDS Card no: 24–0735). The corresponding SAED pattern shows sharp diffraction spots attributed to the polycrystalline nature of PCM (Fig. 5f).

The EDX spectrum of PCz is shown in Fig. S2a (Supplementary files) substantiated that; it is mainly comprised of carbon, nitrogen and oxygen. The weight percentage of carbon (78.98%) is higher than the nitrogen

(11.26%) and oxygen (9.76%). In addition to these, the PCM (Fig. S2b) is qualitatively constituted of various elements such as carbon (C), oxygen (O) and manganese (Mn). The sharp peak reveals the crystalline nature and the amorphous nature also present to some extent. From the results, the carbon is dominant with weight percentage of 69.34% which is higher than the oxygen (17.22%), and manganese (13.44%). The results suggest that the presence of these elements confirms the formation of PCM. In addition to these, the elemental color mapping images of PCM (Fig. S3) revealed the presence of Carbon (blue), Nitrogen (green), Oxygen (fluorescent green) and Manganese (red).

### Cyclic voltammetry study

Cyclic voltammetry (CV) study reveals the HOMO–LUMO energy level to understand the electronic transition for the photo degradation of dyes. When the monomer is polymerized, the HOMO–LUMO gap can significantly changed [35]. In addition to these, the band gap of PCz and MnO<sub>2</sub> were calculated from the analysis. As shown in Fig. 6a, the glassy carbon electrode exhibited an onset potential of oxidation and reduction peak for PCz at +0.29 V and –0.66 V versus NHE. Similarly, the peak for MnO<sub>2</sub>

**Fig. 6** Cyclic voltammtery of (a) PCz (b) MnO<sub>2</sub>

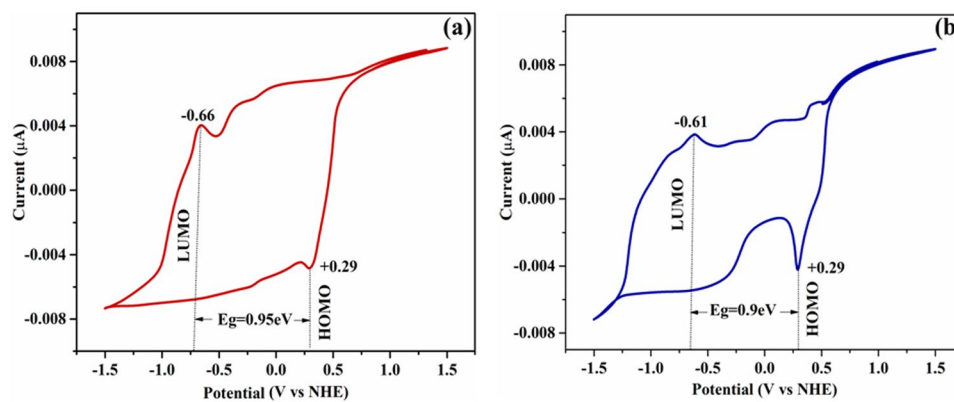


(Fig. 6b) is appeared at +0.29 V (oxidation) and -0.61 V (reduction). The  $E_{\text{HOMO}}$  and  $E_{\text{LUMO}}$  of PCz were calculated as  $-5.04$  eV and  $-4.09$  eV. Similarly, for MnO<sub>2</sub> it is estimated as  $-5.0$  eV and  $-4.14$  eV respectively. The band gap of PCz and MnO<sub>2</sub> calculated from the graph is 0.95 eV and 0.9 eV. The LUMO and HOMO level of PCz is higher than the conduction and valence band of MnO<sub>2</sub>. Therefore, the electrons in the LUMO of PCz can easily migrate into the conduction band of MnO<sub>2</sub> due to the electron donating property of PCz and accepting property of MnO<sub>2</sub> which increases the separation of free charge carriers for the enhanced photo degradation of dyes.

## BET analysis

The physical properties of PCz, PCM, PCM1, PCM2, PCM3 and PCM4 were determined with the nitrogen (N<sub>2</sub>) adsorption–desorption isotherm analysis and illustrated in Fig. S4 (Supplementary files). In view of the Brunauer-Deming-Deming-Teller (BDDT) classification, the isotherm with a hysteresis loops ( $P/P_0 > 0.45$ ) correlated to type IV (H3), indicating the mesoporous nature of the material. The specific surface area, mean pore diameter and total pore volume of PCz, PCM, PCM1, PCM2, PCM3 and PCM4 were listed in Table 1. The surface area of PCz is lowest ( $4.0 \text{ m}^2\text{g}^{-1}$ ), whereas the PCM exhibited the surface area of

**Table 1** Physical properties of PCz, PCM, PCM1, PCM2, PCM3 and PCM4

Material	Surface area	Total pore volume	Mean pore diameter
PCz	4.0	0.039	39.2
PCM	4.8	0.046	33.3
PCM1	7.4	0.084	45.4
PCM2	8.6	0.057	26.9
PCM3	33.8	0.054	8.2
PCM4	27.8	0.070	7.8

$4.8 \text{ m}^2\text{g}^{-1}$ . It is noted that the surface area is increased after the decoration of MnO<sub>2</sub> in PCz matrix. Furthermore, the annealing temperature increased the surface area of PCM1 ( $7.4 \text{ m}^2\text{g}^{-1}$ ), PCM2 ( $8.6 \text{ m}^2\text{g}^{-1}$ ), PCM3 ( $33.8 \text{ m}^2\text{g}^{-1}$ ) and PCM4 ( $27.8 \text{ m}^2\text{g}^{-1}$ ). It is noted that the PCM3 has the larger surface area compared to other materials. The annealing of the material resulted in uniform globular morphology, which presumably increased the surface area. It is noted that the  $\alpha$ -phase dominance led to the enhanced surface area. Therefore, the modification of PCM3 by the effect of annealing enables more active sites for the degradation of dye pollutants.

## Thermal studies

As shown in Fig. S5 (Supplementary files), the PCz exhibited weight loss at two stages. The first one is observed at  $262.6$  °C. It is estimated that 31.4% of the material is lost due to the evaporation of residual water. The second one is observed at  $701.0$  °C with a weight loss of 68.5%. It is observed that the weight loss started to decrease from  $262$  °C and continued up to  $701$  °C, where the total weight of the sample is completely decomposed at  $701$  °C.

However, the PCM (Fig. S5) shows weight loss at two stages; first one is at  $232.7$  °C which is attributed to the degradation of PCz. The second one is observed between  $600$ – $700$  °C. The total weight loss is estimated to 11.6% which shows that the material is not completely oxidized and is more stable. At high temperatures exceeding above  $700$  °C the nanocomposite maintains its stability without any weight loss. Furthermore, it is observed that the PCM is consequently stable above  $868.8$  °C thereby exhibited superior thermal stability than PCz.

The reason for the high thermal stability of PCM is attributed to the following factors such as compact structure, high molecular weight of PCz, strong interaction of MnO<sub>2</sub> with PCz chains. Furthermore, it is important to note that the thermal degradation of PCM starts at much lower



temperature (232.7 °C) than PCz (262 °C) which may be due to the synergistic effect between PCz and MnO<sub>2</sub>. Moreover, the PCz shows sudden weight loss but in the case of PCM it exhibited a gradual weight loss demonstrating the enhanced thermal stability of PCz/MnO<sub>2</sub> nanocomposite than PCz.

## Photo catalytic performance

The photo catalytic performance of PCz, MnO<sub>2</sub>, PCM, PCM1, PCM2, PCM3 and PCM4 is evaluated by using two different organic dyes (RB and MG) as target pollutants. Initially the photo catalytic activity without light illumination or photo catalyst was observed which shows no significant degradation. On the other hand, the degradation was very rapid in the presence of photo catalyst or light illumination (0–30 min) due to the presence of vacant adsorption sites. The degradation is stabilized after 30 min which indicates the completion of the equilibrium.

The degradation efficiency of PCz shows 74.6% (UV) and 78.9% (sunlight) towards RB dye. Similarly, it shows 75.3% (UV) and 77.4% (sunlight) under identical conditions. Besides, MnO<sub>2</sub> exhibited 54.0% (UV) and 67.0% (sunlight) over RB dye. In addition, it shows 65.0% (UV) and 71.0% (sunlight) against MG dye under the same conditions. The degradation efficiency of PCM towards RB dye is 80.6% (UV) and 84.6% (natural sunlight). Correspondingly, the degradation ability of PCM towards MG dye is 83.7% (UV) and 85.4% (natural sunlight). The photo catalytic activity of PCM towards RB dye is 1.08 (UV) and 1.07 (sunlight) times higher than PCz. In the same way, it is 1.11 (UV) and 1.10 (sunlight) times higher than PCz towards MG dye. The pure MnO<sub>2</sub> shows low degradation efficiency towards the RB and MG dyes under UV and

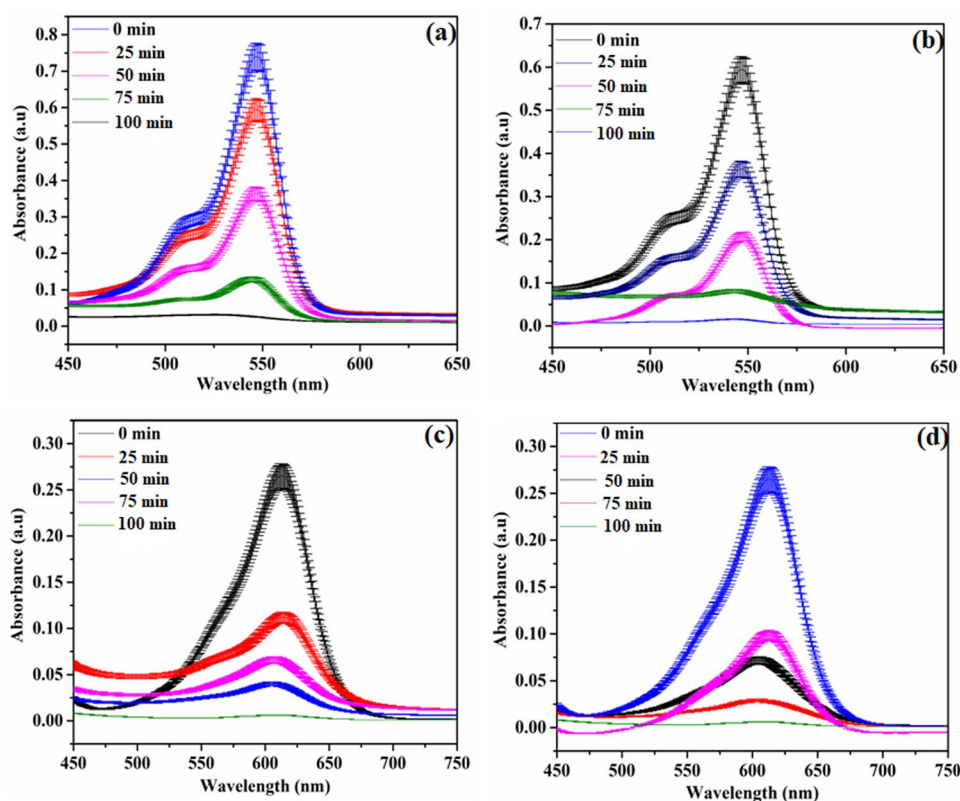
natural sunlight irradiation. However, the photo catalytic performance is increased after the introduction of MnO<sub>2</sub> nanoparticles into PCz matrix because the polycarbazole forms a protective layer on the surface of MnO<sub>2</sub> which improves the separation of electron–hole pairs between PCz and MnO<sub>2</sub>. Furthermore, the dispersion of MnO<sub>2</sub> into polycarbazole matrix improves the adsorption ability. The p-type semiconducting property of MnO<sub>2</sub> depends on hole conductance while polycarbazole as a conjugated polymer is easy to accept electrons. Thus, the electrons excited on the surface is dispersed to polycarbazole, which suppress the recombination of electron–hole pairs and improve the photocatalytic activity of the nanocomposites. Therefore, it is observed that the polycarbazole plays a crucial role in the enhanced photocatalytic activity.

The effect of annealing on the photo catalytic efficiency were evaluated and tabulated in Table 2. From the results, it is observed that the best degradation efficiency was observed for PCM3 towards RB (Fig. 7a, b) dye under UV (96.2%) and natural sunlight (97.9%). Similarly, the photo degradation ability of PCM3 towards MG dye (Fig. 7c, d) is 97.4% (UV) and 98.3% (natural sunlight). The photo catalytic activity of PCM3 towards RB dye is 1.19 (UV) and 1.15 (sunlight) times higher than PCM. In the same way, it is 1.16 (UV) and 1.15 (sunlight) times higher than PCM towards MG dye. The results show that the photo catalytic performance is increased after annealing. The apparent rate constant of PCM3 over RB (Fig. S6a, b) dye is  $3.7 \times 10^{-2} \text{ min}^{-1}$  (UV) and  $3.5 \times 10^{-2} \text{ min}^{-1}$  (natural sunlight). Similarly, it shows  $3.6 \times 10^{-2} \text{ min}^{-1}$  (UV) and  $3.8 \times 10^{-2} \text{ min}^{-1}$  (natural sunlight) towards MG (Fig. S6c, d) dye. Herein, the PCM3 is 1.9 (UV) and 1.2 (natural sunlight) times higher than PCM towards RB dye. In addition to these, the PCM3 is 1.5 (UV) and 1.1 (natural sunlight) times higher than PCM over MG dye.

**Table 2** Degradation % and linear fitting parameters

Catalyst	Dye	Degradation%		Slope		R-Square	
		UV	Sunlight	UV	Sunlight	UV	Sunlight
PCz	RB	74.6	78.9	$2.5 \times 10^{-2}$	$2.4 \times 10^{-2}$	0.9651	0.9734
PCz	MG	75.3	77.4	$2.5 \times 10^{-2}$	$2.5 \times 10^{-2}$	0.8527	0.9487
MnO <sub>2</sub>	RB	54.0	67.0	$1.7 \times 10^{-2}$	$1.9 \times 10^{-2}$	0.9461	0.9446
MnO <sub>2</sub>	MG	72.0	76.0	$1.6 \times 10^{-2}$	$1.9 \times 10^{-2}$	0.9463	0.9631
PCM	RB	80.6	84.6	$2.1 \times 10^{-2}$	$2.9 \times 10^{-2}$	0.9463	0.9860
PCM	MG	83.7	85.4	$2.4 \times 10^{-2}$	$3.4 \times 10^{-2}$	0.9648	0.9581
PCM1	RB	88.7	89.6	$3.1 \times 10^{-2}$	$3.1 \times 10^{-2}$	0.9375	0.9389
PCM1	MG	89.9	90.1	$3.4 \times 10^{-2}$	$3.3 \times 10^{-2}$	0.9794	0.9855
PCM2	RB	92.1	91.3	$3.4 \times 10^{-2}$	$2.8 \times 10^{-2}$	0.9751	0.9616
PCM2	MG	91.8	93.8	$3.5 \times 10^{-2}$	$2.8 \times 10^{-2}$	0.9473	0.9737
PCM3	RB	96.2	97.9	$3.7 \times 10^{-2}$	$3.5 \times 10^{-2}$	0.9239	0.9736
PCM3	MG	97.4	98.3	$3.6 \times 10^{-2}$	$3.8 \times 10^{-2}$	0.9790	0.9891
PCM4	RB	93.8	95.5	$2.7 \times 10^{-2}$	$3.3 \times 10^{-2}$	0.9751	0.9224
PCM4	MG	94.3	96.0	$3.1 \times 10^{-2}$	$3.0 \times 10^{-2}$	0.9273	0.9811

**Fig. 7** UV–vis absorption spectrum of PCM3 towards various irradiation time under (a) UV of RB (b) sunlight of RB (c) UV of MG (d) direct sunlight irradiation of MG dye



From the results, it is evidenced that the rate constant of PCM3 is higher than PCM under light irradiation. Therefore, the annealing of material enhanced the photo catalytic performance. The photo degradation percentage and rate constant values of PCz, MnO<sub>2</sub>, PCM, PCM1, PCM2, PCM3 and PCM4 were summarized in Table 2.

The photo catalytic activity can be quantitatively investigated by fitting the degradation data using kinetic model. As illustrated in Fig. S6 (Supplementary file), the linear relationship between  $\ln(C_0/C_t)$  versus irradiation time corroborate the feasibility of this model. The correlation coefficient value of PCz, MnO<sub>2</sub>, PCM, PCM1, PCM2, PCM3 and PCM4 over RB dye under UV (Fig. S6a) and natural sunlight (Fig. S6b) as well as the MG dye under UV (Fig. S6c) and direct sunlight (Fig. S6d) is near to 1. Therefore, the result indicates that the PCM and the annealed samples exhibited pseudo first order kinetics.

The result shows that the PCz and MnO<sub>2</sub> are the promising material which has the potential to degrade the dyes under light irradiation in 150 min. The PCz is a photoactive material which suppress the electron–hole recombination for the photo degradation of the textile dyes. Furthermore, the high degradation efficiency of PCM over pristine PCz is governed by the following facts: first, it is due to the enhanced charge separation of photogenerated electrons and holes achieved by the synergistic effect between PCz and MnO<sub>2</sub>. The results agreed well with the reported

studies [36]. Moreover, the PCz facilitates the separation of light induced charge carriers between PCz and MnO<sub>2</sub>. Second, the morphology of PCM compared to PCz shows good dispersion of MnO<sub>2</sub> nanoparticles which results in the high surface area accessible to the light sources for the high degradation efficiency [37]. Third, the surface area of PCM is 1.84 times higher than PCz. It is noteworthy that the surface area produces innumerable photo excited electron–hole pairs required for the superior photo degradation process under light irradiation [38]. Finally, the pore volume and pore diameter of PCM is 2.1 and 1.1 times larger than PCz. The earlier studies reveal that the pore properties play a vital role in facilitating the chemical reactions to takes place by transporting the reactant or product molecules to move everywhere [39, 40] hence; the PCM shows improved photo catalytic activity.

In addition, photocatalytic performance of PCM3 is observed to be higher than PCM1, PCM2, PCM4, PCM, PCz and MnO<sub>2</sub>. The PCM degraded the dye in 150 min while the PCM3 degraded the dye in 100 min with a high photo-catalytic efficiency. The reason for the high performance photocatalysis are. Firstly, the increase in the temperature results in larger grain size (observed from SEM analysis) and higher crystallinity (observed from XRD) which decreases the electron–hole recombination and facilitates the separation of electron–hole pairs and thereby increases the photo catalytic activity. Secondly, the conductivity of the sample significantly improved after

annealing at higher temperature (600 °C) which enhances the number of light induced charge carriers for enhanced photo catalytic activity. Thirdly, the surface area of PCM3 (33.8 m<sup>2</sup>/g) is higher than the other annealed samples which influence the photo catalytic performance. Furthermore, the annealed samples can produce a number of OH, H<sub>2</sub>O and O<sub>2</sub> radicals which react with the light generated electron-holes for producing more number of active radicals for enhanced photo catalytic activity. Furthermore, to evaluate the efficiency of the photo catalyst it is compared with the reported photo catalyst [41–48] and summarized in Table 3. It is observed that the synthesized PCM3 demonstrated high degradation efficiency than the other reported photo catalyst.

Photo catalytic degradation of pollutants results in intermediates which cause more harm than the pollutants. Hence, to identify whether the synthesized material can break down the pollutants into harmless products the TOC analysis is performed. After 100 min of irradiation, the PCM3 exhibited the TOC removal efficiencies against RB (47.21) and MG (62.13%) dyes under UV light. In the same way, it shows 76.14 (RB) and 85.66% (MG) under natural sunlight illumination. It is observed that the PCM effectively converted the pollutants into small products during photo catalytic degradation of the organic dyes.

### Possible mechanism of the enhanced photo catalytic activity

In order to investigate the enhanced photo catalytic activity comprehensively photoluminescence spectrum (PL), electrochemical impedance spectroscopy (EIS), cyclic voltammetry (CV) and quenching experiment were carried out. The PL spectrum (Fig. 8a) is used to investigate the migration and decoupling of light induced charge carriers (e<sup>-</sup>/h<sup>+</sup>) on the surface of the photo catalyst which is related to the excitation wavelength. The PCM

is excited at a wavelength of 360 nm which shows two kinds of high emission peaks, first one is at 343.9 and the second one is at 356.5 nm suggesting high recombination efficiency. Besides, PCM3 is excited at 360 nm which exhibited low emission peaks at 344.9 and 355.5 nm. Universally speaking, the high intensity peak leads to high recombination rate and the low intensity peak leads to low recombination rate which enables more free charge carriers for the improved photo catalytic performance [49, 50]. Therefore, the low intensity peak obtained for PCM3 leads to the suppression of recombination of e<sup>-</sup>/h<sup>+</sup> pairs which favors the photo degradation of the dyes.

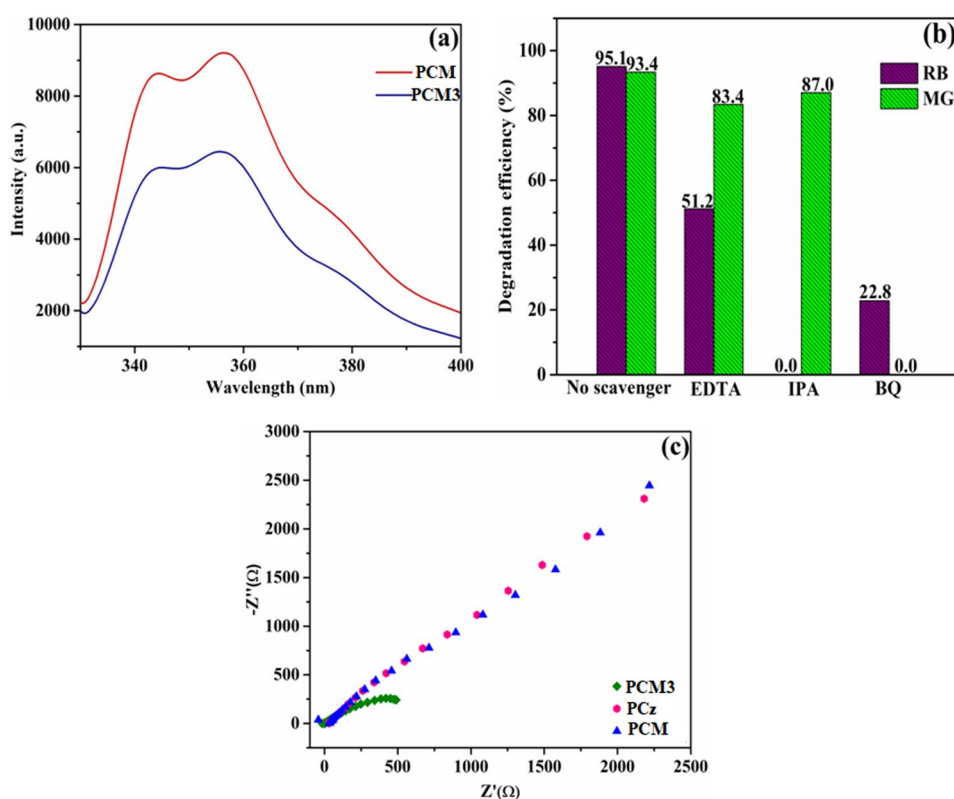
Furthermore, to determine the involvement of radicals in the photo catalytic activity, the quenching experiment is performed. As shown in Fig. 8b, the degradation percentage of PCM3 towards RB dye is decreased from 95.1 (no scavenger) to 51.2 (EDTA), 22.8 (BQ) and 0 (IPA) suggesting that the degradation is greatly promoted by IPA, which implies that the hydroxyl radicals favored the photo catalytic activity. On the other hand, the photo degradation percentage of PCM3 against MG dye is decreased from 93.4 (no scavenger) to 83.4 (EDTA), 0 (BQ) and 87.0 (IPA) indicating that the superoxide (BQ) is the main active species involved in the degradation. Therefore, it is disclosed that the degradation of RB dye is influenced by hole (h<sup>+</sup>) and superoxide (\*O<sub>2</sub><sup>-</sup>) radicals. In addition hydroxyl ((OH\*)) and hole (h<sup>+</sup>) were the minor radicals during the degradation of MG dye.

The position of conduction band (CB) and valence band (VB) are very important to understand the enhanced photo degradation mechanism in detail. It is interesting to observe that the band gap of PCz (0.95 eV) and MnO<sub>2</sub> (0.9 eV) are almost equal which can form heterojunction for the enhanced carrier separation. Moreover, the CB (-0.66) of PCz is more negative than the CB (-0.61) of MnO<sub>2</sub> which is thermodynamically favor for the migration of photocreated electron–hole pairs. Subsequently, the light induced charge separation was rapid and the recombination rate was relatively slow which is beneficial for the photo catalytic activity.

**Table 3** Comparison of photocatalytic performance of PCM3 with reported material

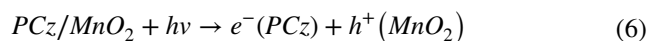
Name of the photocatalyst	Name of the dye	Irradiation source	Degradation % or rate constant (K <sub>app</sub> ) min <sup>-1</sup>	Ref
Sm/CeO <sub>2</sub>	RB	UV	89	[41]
RGO/TiO <sub>2</sub>	RB	sunlight	94	[42]
ZnO	RB	UV	80	[43]
NaNbO <sub>3</sub> /ZnO	RB	sunlight	75	[44]
PCM3	RB	UV	96.2	Present work
PCM3	RB	Sunlight	97.9	Present work
PANI/ZnO	MG	UV	89	[45]
PAZ/TiO <sub>2</sub>	MG	sunlight	93	[46]
PANI/TiO <sub>2</sub>	MG	UV	92.2	[47]
GG/Al <sub>2</sub> O <sub>3</sub>	MG	sunlight	90	[48]
PCM3	MG	UV	97.4	Present work
PCM3	MG	Sunlight	98.3	Present work

**Fig. 8** a) PL spectrum of PCM and PCM3 b) Scavenging activity b) EIS spectra of PCz, PCM and PCM3

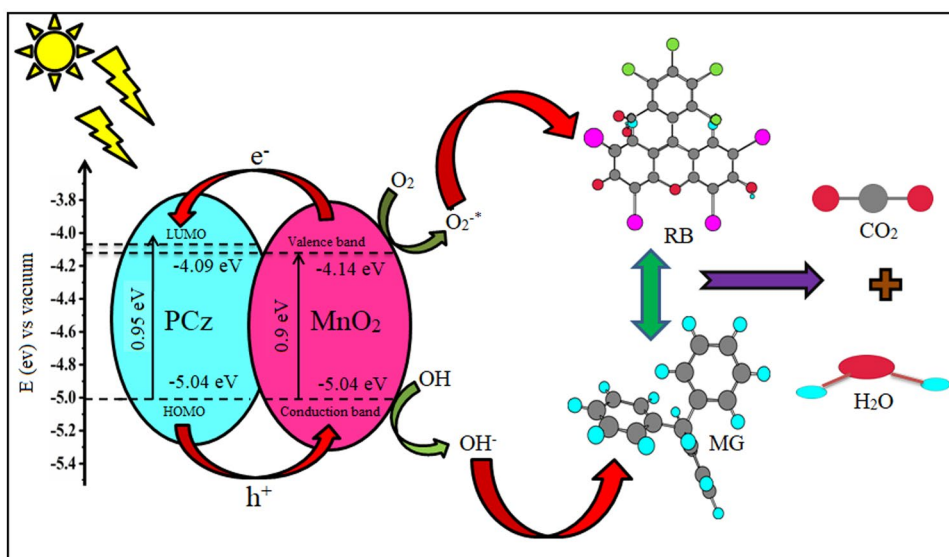


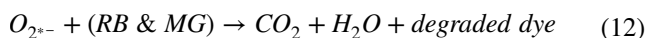
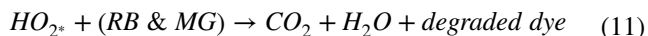
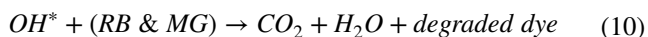
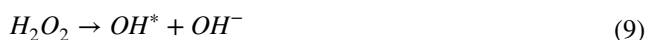
Generally, EIS is employed to measure the migration of light induced charge carriers. Usually, the smaller semicircular arc indicates lesser interfacial resistance and faster electron migration [51–53]. As illustrated in Fig. 8c, the PCM3 exhibited smaller arc radius related to the lowest resistance and rapid migration of charges. It is observed that the photocatalytic performance of PCM3 is higher than PCM and PCz. The photocatalytic mechanism of PCz/MnO<sub>2</sub> nanocomposite against RB and MG dyes under various light illumination is graphically illustrated in Scheme 2

Apart from these, the combined effect of PCz with MnO<sub>2</sub> results in the elevated photocatalytic performance. Therefore the mechanism for the photocatalytic activity is summarized as follows:



**Scheme 2** The photocatalytic mechanism of PCz/MnO<sub>2</sub> nanocomposite against RB and MG dyes under various light illumination





In conclusion, the CV, DRS, PL and EIS studies demonstrated that the decoupling of the free charge carriers is very rapid which may be the prime cause for the enhanced photo catalytic performance. Apart from these, some other factors also involved in enhancing the photo catalytic activity such as high surface area, pore size, crystallinity and the lesser degree of agglomeration.

## Stability and reusability

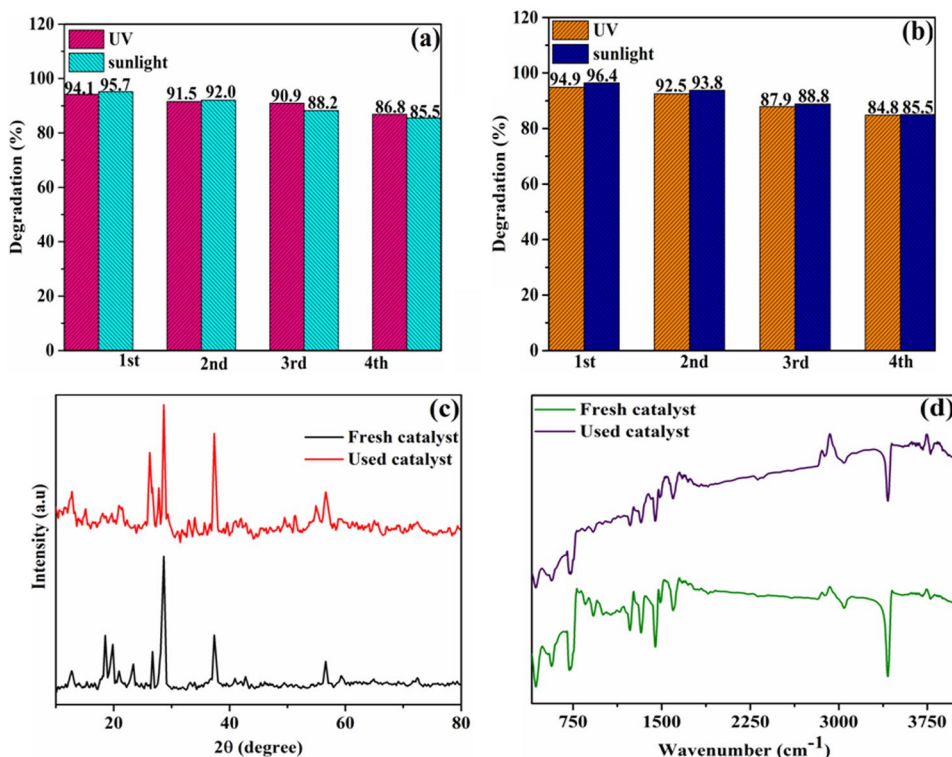
Stability and reusability is imperative for the photo catalyst which determines the practical feasibility for the commercial applications. As illustrated in Fig. 9a, the photo catalytic efficiency (first cycle) of PCM3 over RB dye is 94.16 (UV) and 95.75% (natural sunlight). In the same way, the photo catalytic efficiency of PCM3 over MG dye (Fig. 9b) under the same conditions is 94.96 (UV) and 96.41% (natural sunlight). The

degradation efficiency after the fourth consecutive cycle is 86.84 (UV) and 85.53% (natural sunlight) towards RB dye. Similarly it shows 84.88 (UV) and 85.05% (natural sunlight) towards MG dye. The result evidenced a little decrease in the photo catalytic activity after each cycle. The minimal loss in the photo catalytic activity for each cycle is 4–6% which shows that the material is remained unchanged and is recovered by regenerating with deionized water. The decrease is due to residual dyes shield the texture of photo catalyst which absorbs the reactive centers of the photo catalyst. In addition, the used material was characterized by XRD (Fig. 9c) and FTIR (Fig. 9d) technique. The phase and the structure of the material are compared with the material before and after treatment which shows no significant change. The repeated cyclic runs confirm that the catalytic reactions took place rather than the chemical reaction. Furthermore, the synthesized PCz/MnO<sub>2</sub> nanocomposite is more stable in the cyclic runs as well as in the structure which is considered as a potential candidate for the practical applications.

## Textile effluent sample analysis

The PCM3 is treated with the textile effluent sample to investigate for the practical applications. The COD analysis is performed to determine the amount of oxygen needed to contribute the CO<sub>2</sub> and H<sub>2</sub>O during the mineralization of the organic pollutants. The mineralization of PCM3 towards real life time sample is 63.8% in 120 min. Furthermore, the degradation efficiency of

**Fig. 9** Recycling test of PCM towards (a) RB dye under UV and direct sunlight irradiation (b) MG dye under UV and direct sunlight irradiation. XRD pattern of (a) PCM (fresh and used) (c) FTIR spectra of PCM (fresh and used)



the PCM3 after 120 min of photo catalytic treatment is 78%. The COD removal rate and the degradation efficiency results indicate that the PCM3 is suitable for purifying the waste water from the industries. The photo degradation of PCM3 towards textile effluent sample under direct sunlight is shown in Fig. S7.

## Conclusion

The PCz and PCz/MnO<sub>2</sub> nanocomposite were successfully prepared by facile in situ chemical polymerization process. The material was confirmed by well determined peaks revealed by spectral analysis. The PCM shows the band gap of 3.54 eV which evidenced that the material is active beneath light illumination. The weight percentage of sample remained after the thermal degradation of PCz at 702.02 °C is 0% and PCM at 868.68 °C is 88.4% which evidenced the high thermal stability. The CV study reveals that the HOMO and LUMO level of PCz is higher than the conduction and valence band of MnO<sub>2</sub> which brought great benefit for the enhanced photo catalytic activity. The EIS spectra of PCM exhibited shorter semicircular arcs which provide lower interfacial resistance and a faster electron transfer process. Photo degradation efficiency of PCM3 ( $\alpha$ -MnO<sub>2</sub>-phase) was superior to the other phase transformed samples ( $\beta$ ,  $\gamma$  phases). The PCz played an important role in the light harvesting and light induced charge carriers of MnO<sub>2</sub>. The outstanding photo catalytic performance is influenced by number of factors such as low degree of aggregation, small particle size of the material, rapid recombination efficiency for generating electron–hole pairs. Furthermore the material was reused for up to four cycles which demonstrates the reliability for practical applications. According to the scavenging activity, the electron–hole pairs were the key species involved in the photo degradation of RB and MG dyes. The present work provides a promising potential photo catalyst for the removal of various textile dyes present in the industrial waste water.

**Supplementary information** The online version contains supplementary material available at <https://doi.org/10.1007/s10965-021-02791-9>.

**Acknowledgements** The authors are profoundly grateful to the STIC Cochin and Central research lab, Vellalar College of technology, Erode for providing the research facilities such as XRD, SEM, TGA-DTA, HR-TEM, FTIR, UV studies. The FESEM, color mapping studies were provided by PSG TECHS COE INDUTECH, Coimbatore. The CV studies were performed at CECRI; Karaikudi and UV-DRS studies were done at Alagappa University, Karaikudi.

**Funding** The author D. John Williams (UGC-RGNFD-2016–17-TAM-2904) owe a debt of gratitude to the University Grants Commission (UGC)—Rajiv Gandhi National Fellowship for Disabled (RGNFD) New Delhi for the financial assistance through the Junior and Senior Research Fellowship (JRF-SRF).

## Declarations

**Conflict of interest** The authors declare that they have no conflict of interest.

## References

- Zhong X, Dai Z, Qin F, Li J, Yang H, Lu Z, Liang Y, Chen R (2015) Ag-decorated Bi<sub>2</sub>O<sub>3</sub> nanospheres with enhanced visible-light driven photo catalytic activities for water treatment. *Rsc Adv* 5:69312–69318. <https://doi.org/10.1039/c5ra12779c>
- Xue J, Li X, Ma S, Xu P, Wang M, Ye Z (2018) Facile fabrication of BiOCl/RGO/protonated g-C<sub>3</sub>N<sub>4</sub> ternary nanocomposite as Z-scheme photo catalyst for tetracycline degradation and benzyl alcohol oxidation. *J Mater Sci* 54:1275–1290. <https://doi.org/10.1007/s10853-018-2880-5>
- Aly KI, Sayed MM, Mohamed MG, Kuo SW, Younis O (2020) A facile synthetic route and dual function of network luminescent porous polyester and copolyester containing porphyrin moiety for metal ions sensor and dyes adsorption. *Microporous Mesoporous Mater* 298:110063. <https://doi.org/10.1016/j.micromeso.2020.110063>
- Su C (2017) Environmental implications and applications of engineered nanoscale magnetite and its hybrid nanocomposites: A review of recent literature. *J Hazard Mater* 322:48–84. <https://doi.org/10.1016/j.jhazmat.2016.06.060>
- Nasirian S, Maghaddam HM (2014) Hydrogen gas sensing base on polyaniline/anatase titania nanocomposite. *Int J Hydrog Energy* 39:630–642. <https://doi.org/10.1016/j.ijhydene.2013.09.152>
- Papinutti L, Mouso N, Forchiassin F (2006) Removal and degradation of the fungicide dye malachite green from aqueous solution using the system wheat bran-fomes sclerodermeus. *Enzyme Microb Technol* 39:848–853. <https://doi.org/10.1016/j.enzmictec.2006.01.013>
- Kim S, Choi W (2002) Kinetics and mechanisms of photo catalytic degradation of (CH<sub>3</sub>)<sub>n</sub>NH<sub>4-n</sub><sup>+</sup> (0 < n < 4) in TiO<sub>2</sub> suspension: the role of OH radicals. *Environ Sci Technol* 36:2019–2025. <https://doi.org/10.1021/es015560s>
- Wong CC, Chu W (2003) The hydrogen peroxide-assisted photo catalytic degradation ofalachor in TiO<sub>2</sub> suspensions. *Environ Sci Technol* 37:2310–2316. <https://doi.org/10.1021/es020898n>
- Sharma S, Dutta V, Sing P, Raizada P, Rahmani-Sani A, Hosseini-Bandegharai A, Thakur VK (2019) Carbon quantum dot supported semiconductor photocatalysts for efficient degradation of organic pollutants in water: a review. *J Clean Prod* 228:755–769. <https://doi.org/10.1016/j.jclepro.2019.04.292>
- Hietmann AP, Rocha IC, Pereira IM, Oliveira LCA, Patricio PSO (2019) Nanoparticles of niobium oxyhydroxide incorporated in different polymers for photocatalytic degradation of dye. *J Polym Res* 26:159. <https://doi.org/10.1007/s10965-019-1824-3>
- Ossoss KM, Hassan MER, Al-Hussaini AS (2019) Novel Fe<sub>2</sub>O<sub>3</sub>@PANI-o-PDA core shell nanocomposites for photocatalytic degradation of aromatic dyes. *J Polym Res* 26:199. <https://doi.org/10.1007/s10965-019-1856-8>
- Regonini D, Bowen CR, Jaroenworarluck A, Stevens R (2013) A review of growth mechanism, structure and crystallinity of anodized TiO<sub>2</sub> nanotubes. *Mater Sci Eng R* 74:377–406. <https://doi.org/10.1016/j.mser.2013.10.001>
- EL-Mahdy AFM, Zakaria MB, Wang H-X, Chen T, Yamauchi Y, Kuo S-W (2020) Heteroporous bifluorenylidene-based covalent organic frameworks displaying exceptional dye

- adsorption behavior and high energy storage J.Mater. Chem.A.8:25148–25155. <https://doi.org/10.1039/D0TA07281H>
14. Mohamed MG, Atayde EC Jr, Matsagar BM, Na J, Yamauchi Y, Wu KC-W, Kuo SW (2020) Construction Hierarchically Mesoporous/Microporous Materials Based on Block Copolymer and Covalent organic frame work. *J Taiwan Inst Chem Eng* 112:180–192. <https://doi.org/10.1016/j.jtice.2020.06.013>
  15. Kashyap J, Ashraf SM, Riaz U (2017) Highly efficient photo catalytic degradation of amido black 10B dye using polycarbazole-decorated TiO<sub>2</sub> nanohybrids. *ACS Omega* 2:8354–8365. <https://doi.org/10.1021/acsomega.7b01154>
  16. Sun W, Sun W, Zhuo Y, Chu Y (2011) Facile synthesis of Cu<sub>2</sub>O nanocube/polycarbazole composites and their high visible-light photo catalytic properties. *J Solid State chem* 184:1638–1643. <https://doi.org/10.1016/j.jssc.2011.03.055>
  17. Praveena P, Dhanavel S, Sangamithirai D, Narayanan V, Stephen A (2018) Visible light driven photo catalytic degradation of methylene blue using novel camphor sulfonic acid doped polycarbazole/g-C<sub>3</sub>N<sub>4</sub> nanocomposite. *AIP conf. Proc.* 1942:050131–1–050131–4. <https://doi.org/10.1063/1.5028762>
  18. Xu H, Zhang J, Chen Y, Lu H, Zhuang J, Li J (2014), Synthesis of polyaniline-modified MnO<sub>2</sub> composite nanorods and their photocatalytic application. *Mater. Lett.* 117: 21–23. <https://doi.org/10.1016/j.matlet.2013.11.089>
  19. Zhang L, Jamal R, Zhao Q, Wang M, Abdiryim T (2015) Preparation of PEDOT/GO, PEDOT/MnO<sub>2</sub> and PEDOT/GO/MnO<sub>2</sub> nanocomposites and their application in catalytic degradation of methylene blue. *Nanoscale Res Lett* 10:148. <https://doi.org/10.1186/s11671-015-0859-6>
  20. Zhou Q, Zhang L, Zuo P, Wang Y, Yu Z (2018) Enhanced photo catalytic performance of spherical BiOI/MnO<sub>2</sub> composite and mechanism investigation. *RSC Adv* 8:36161–36166. <https://doi.org/10.1039/c8RA06930a>
  21. Ma M, Yang Y, Chen Y, Wu F, li W, Lyu P, Ma Y, Tan W, Huang W (2019) Synthesis of hollow flower like Fe<sub>3</sub>O<sub>4</sub>/MnO<sub>2</sub>/Mn<sub>3</sub>O<sub>4</sub> magnetically separable microspheres with valence heterostructure for dye degradation. *Catalysts* 9:589–601. <https://doi.org/10.3390/catal9070589>
  22. Yang P, Wang SQ, Ando M, Murase N (2013) CdSe/Cd<sub>1-x</sub>Zn<sub>x</sub>S core/shell quantum dots with tunable emission: growth and morphology evolution. *J Mater Sci* 48:651–658
  23. Sethi R, Kumar L, Sharma K, Pandey AC (2010) Tunable visible emission of Ag-doped CdZnS alloy quantum dots. *Nanoscale Res Lett* 5:96–102
  24. Macit H, Sen S, Sacak M (2005) Electrochemical synthesis and characterization of polycarbazole. *J Appl Polym Sci* 96:894–898. <https://doi.org/10.1002/app.21532>
  25. Zia J, Aazam ES, Riaz U (2020) Synthesis of nanohybrids of polycarbazole with α-MnO<sub>2</sub> derived from brassica oleracea: A comparison of photocatalytic degradation of an antibiotic drug under microwave and UV irradiation. *Environ Sci Pollut Res* 27:24173–24189. <https://doi.org/10.1007/s11356-020-08149-w>
  26. Shakir M, Noor-e-iram KMS, Al-resayes SI, Khan AA, Baig U (2014) Electrical conductivity, isothermal stability and ammonia sensing performance of newly synthesized and characterized organic-inorganic polycarbazole-titanium dioxide nanocomposite. *Ind Eng Chem Res* 53:8035–8044. <https://doi.org/10.1021/ie404314q>
  27. Riaz U, Ashraf SM, Khan N (2011) Effects of surfactants on microwave-assisted solid state intercalation of poly (carbazole) in bentonite. *J Nanpart Res* 13:6321–6331. <https://doi.org/10.1007/s11051-011-0611-9>
  28. Tao Y, Zhang K, Zhang Z, Cheng H, Jiao C, Zhao Y, Xu W (2016) Enhanced electro chromic properties of donor-acceptor polymers via TiO<sub>2</sub> composite. *Polymer* 91:98–105. <https://doi.org/10.1016/j.polymer.2016.03.060>
  29. Iram NE, Khan MS, Jolly R, Arshad M, Alam M, Alam P, Khan RH, Firdaus F (2015) Interaction mode of polycarbazole-titanium dioxide nanocomposite with DNA: Molecular docking simulation and in-vitro antimicrobial study. *J Photochem Photobiol B* 153:20–32. <https://doi.org/10.1016/j.jphotochem.2015.09.001>
  30. Kumar A, Kumar R, Pandey G (2018) Synthesis, characterization of Titania/Polyaniline/GO nanocomposites, and its photocatalytic activity under visible light. *Macromol Symp* 379:1600192–1600200. <https://doi.org/10.1002/masy.201600192>
  31. Duran P, Capel F, Tartaj J, Moure C (2002) A strategic two-stage low-temperature thermal processing leading to fully dense and fine-grained doped-ZnO varistors. *Adv Mater* 14:137–141. [https://doi.org/10.1002/1521-4095\(20020116\)14:2%3C137::AID-ADMA137%3E3.0.CO;2-7](https://doi.org/10.1002/1521-4095(20020116)14:2%3C137::AID-ADMA137%3E3.0.CO;2-7)
  32. Pan ZW, Li Y, Hou X, Yan JJ, Wang CW (2014) Effect of annealing temperature on the photocatalytic activity of CdS modified TNAs/glass nanotube arrays. *Physica E* 63:1–7. <https://doi.org/10.1016/j.apsusc.2017.02.255>
  33. Perera SD, Mariano RG, Vu K, Nour N, Seitz O, Chabal Y, Balkus KJ Jr (2012) Hydrothermal synthesis of graphene-TiO<sub>2</sub> nanotube composites with enhanced photo catalytic activity. *ACS Catal* 2:949–956. <https://doi.org/10.1021/cs200621c>
  34. Muchuwani E, Sathiaraj TS, Nyakotoy H (2018) Effect of annealing on the microstructural, optical and electric properties of ZnO nanowires by hydrothermal synthesis for transparent electrode fabrication. *Mater Sci Eng B Solid State Mater Adv Technol* 227:68–73
  35. Mohamed MG, Lee CC, El-Mahdy AFM, Luder J, Yu MH, Li Z, Zhu Z, Chueh CC, Kuo SW (2020) Exploitation of two-dimensional conjugated covalent organic frameworks based on tetraphenylethylene with bicarbazole and pyrene units and applications in perovskite solar cells. *J Mater Chem A* 8:11448–11459. <https://doi.org/10.1039/D0TA02956D>
  36. Xu K, Feng J (2017) Superior photocatalytic performance of LaFeO<sub>3</sub>/g-C<sub>3</sub>N<sub>4</sub> heterojunction nanocomposite under visible light irradiation. *RSC Adv* 7:45369–45376. <https://doi.org/10.1039/C7RA08715B>
  37. Yu HG, Lee SC, Yu JG, Ao CH (2006) Photo catalytic activity of dispersed TiO<sub>2</sub> particles deposited on glass fibers. *J Mol Catal A* 246:206–211. <https://doi.org/10.1016/j.molcata.2005.11.007>
  38. Sadehgzadeh-Attar A (2018) Efficient photo catalytic degradation of methylene blue dye by SnO<sub>2</sub> nanotubes synthesized at different calcinations temperatures. *Sol Energy Mat Sol C* 183:16–24. <https://doi.org/10.1016/j.solmat.2018.03.046>
  39. Yu JG, Yu HG, Cheng B, Zhao XJ, Zhang QJ (2006) Preparation and photo catalytic activity of mesoporous anatase TiO<sub>2</sub> nanofibers by a hydrothermal method. *J Photochem Photobiol A* 182:121–127. <https://doi.org/10.1016/j.jphotochem.2006.01.022>
  40. Yu JG, Yu XX, Huang BB, Zhang XY, Dai Y (2009) Hydrothermal synthesis and visible-light photo catalytic activity of novel cage-like ferric oxide hollow spheres. *Cryst Growth Des* 9:1474–1480. <https://doi.org/10.1021/cg800941d>
  41. Chahal S, Rani N, Kumar A, Kumar P (2020) Electronic structure and photocatalytic activity of samarium doped cerium oxide nanoparticles for hazardous rose bengal dye degradation. *Vacuum* 172:109075. <https://doi.org/10.1016/j.vacuum.2019.109075>
  42. Rosy A, Kalpana G (2018) Influence of RGO/TiO<sub>2</sub> nanocomposite on photo-degrading rhodamineB and rose bengal dye pollutants. *Bull Mater Sci* 41:83–91. <https://doi.org/10.1007/s12034-018-1598-y>
  43. Vidya C, Chandra prabha MN, Antony Raj MAL (2016) Green mediated synthesis of zinc oxide nanoparticles for the photocatalytic degradation of rose bengal dye. *Environ Nanotechnol Monit Manag* 6:134–138. <https://doi.org/10.1016/j.enmm.2016.09.004>
  44. Farooq U, Phul R, Alshehri SM, Ahmed J, Ahmad T (2019) Electrocatalytic and enhanced photocatalytic applications of sodium niobate nanoparticles developed by citrate precursor route. *Sci Rep* 9:1–17. <https://doi.org/10.1038/s41598-019-40745-w>

45. Eskizeybek V, Sari F, Gulce H, Gulce A, Avci A (2012) Preparation of the new polyaniline/ZnO nanocomposite and its photocatalytic activity for degradation of methylene blue and malachite green dyes under UV and natural sunlight irradiations. *Appl Catal B* 119–120:197–206. <https://doi.org/10.1016/j.apcatb.2012.02.034>
46. Pradeeba SJ, Sampath K, Ramadevi A (2019) Photocatalytic degradations of methylene blue, malachite green and Bismarck brown using poly(azomethine)/TiO<sub>2</sub> nanocomposite. *Clust Comput* 22:3893–3909. <https://doi.org/10.1007/s10586-018-2505-4>
47. Sarmah S, Kumar A (2011) Photocatalytic activity of polyaniline-TiO<sub>2</sub> nanocomposites. *Indian J Phys* 85:713–726. <https://doi.org/10.1007/s12648-011-0071-1>
48. Pathania D, Katwal R, Sharma G, Naushad M, Khan MR, Ala'ah H (2016) Novel guar gum/Al<sub>2</sub>O<sub>3</sub> nanocomposite as an effective photocatalyst for the degradation of malachite green dye. *Int J Biol Macromol* 87:366–374. <https://doi.org/10.1016/j.ijbiomac.2016.02.073>
49. Yu JC, Yu J, Ho W, Jiang Z, Zhang L (2002) Effects of F<sup>-</sup> doping on the photo catalytic activity and microstructures of nanocrystalline TiO<sub>2</sub> powders. *Chem Mater* 14:3808–3816. <https://doi.org/10.1021/cm020027c>
50. Wu R, Song H, Luo N, Ji G (2018) Hydrothermal preparation of 3D flower like BiPO<sub>4</sub>/Bi<sub>2</sub>WO<sub>6</sub> microsphere with enhanced visible-light photo catalytic activity. *J Colloid Interface Sci* 524:350–359. <https://doi.org/10.1016/j.jcis.2018.03.031>
51. Huang H, He Y, Lin Z, Kang L, Zhang Y (2013) Two novel bi-based borate photo catalysts: crystal structure, electronic structure, photo electrochemical properties and photo catalytic activity under simulated solar light irradiation. *J Phys Chem C* 117:22986–22994. <https://doi.org/10.1021/jp4084184>
52. Shao B, Liu Z, Zeng G, Wu Z, Liu Y, Cheng M, Chen M, Liu Y, Zhang W, Feng H (2018) Nitrogen-doped hollow mesoporous carbon spheres modified g-C<sub>3</sub>N<sub>4</sub>/Bi<sub>2</sub>O<sub>3</sub> direct dual semiconductor photo catalytic system with enhanced antibiotics degradation under visible light. *ACS Sustain Chem Eng* 6:16424–16436. <https://doi.org/10.1021/acssuschemeng.8b03480>
53. Shao B, Liu X, Liu Z, Zeng G, Liang Q, Cheng C, Zhang YW, Liu Y, Gong S (2019) A novel double Z-scheme photo catalyst Ag<sub>3</sub>PO<sub>4</sub>/Bi<sub>2</sub>S<sub>3</sub>/Bi<sub>2</sub>O<sub>3</sub> with enhanced visible-light photo catalytic performance for antibiotic degradation. *Chem Eng J* 368:730–745. <https://doi.org/10.1016/j.cej.2019.03.013>

**Publisher's Note** Springer Nature remains neutral with regard to jurisdictional claims in published maps and institutional affiliations.